Strain-confinement mechanism in mesoscopic quantum disks based on piezoelectric materials

C. Rivera,[1,*] U. Jahn,[2] T. Flissikowski,[2] J. L. Pau,[1] E. Muñoz,[1] and H. T. Grahn[2]

[1]*ISOM and Departamento de Ingeniería Electrónica, ETSI Telecomunicación, Universidad Politécnica de Madrid, Ciudad Universitaria, 28040 Madrid, Spain*

[2]*Paul-Drude-Institut für Festkörperelektronik, Hausvogteiplatz 5-7, D-10117 Berlin, Germany*

A theoretical study of the effect of inhomogeneous strain in piezoelectric materials is presented. It is shown that for deformation potentials opposite to strain-induced piezoelectric potentials, electrons and holes can drift in opposite directions, both in the in-plane and growth directions. The resultant potential will dramatically affect the confinement of carriers in mesoscopic quantum structures. In this case, states spatially separated in the in-plane direction can be formed, giving rise to unusual optical properties. The proposed model allows for the interpretation of experimental results obtained for (Al,Ga)N/GaN nanocolumnar structures, namely, the dependence of the luminescence intensity on the well thickness, an unusual spectral line broadening, and long lifetime contributions. This model aims to provide design rules to enhance the radiative efficiency in this type of structure.

I. INTRODUCTION

Recent advances in device fabrication have allowed the development of novel nanometric scale structures, such as quantum disks self-formed on lattice-mismatched substrates, or devices in which additional lateral confinement potentials have been formed using high-resolution lithography and crystal growth on masked or etched substrates.[1–4] The properties of these structures have been studied extensively from both the microscopic and macroscopic points of view. However, new behaviors not previously treated in the literature can appear in the intermediate region between the two limiting microscopic and macroscopic cases. An interesting phenomenon, which can affect the optical and electrical properties of mesoscopic systems, is the strain inhomogeneity. The strain inhomogeneity leads to local differences in the band gap, which in turn can be responsible for a variety of carrier confinement situations. We focus our attention on a typical mesoscopic structure where quantum disks are embedded.[5] Since quantum wells are grown pseudomorphically and because of the strain relaxation or strain difference at the free surface (air-material or material-material interface), a strain inhomogeneity is created in the in-plane direction of each quantum well. This effect cannot be neglected when lateral dimensions of the structure are comparable with the spatial variations in the strain field. The size of lateral confinement in these structures usually varies in the mesoscopic range, between the value of the exciton Bohr radius and hundreds of nanometers, depending on the device fabrication technique. If polarization properties are also present in the used materials, the influence of in-plane strain inhomogeneities on the carrier distribution can be even more dramatic due to the existence of spatially dependent built-in fields. This effect of strain on carrier confinement, including polarization fields, is a mechanism which will be called hereafter strain confinement. This mechanism was already proposed by one of the authors (C. Rivera).[6]

Recently, nanocolumnar structures using III-nitrides, with lateral diameters between 20 and 120 nm, have been fabri-cated by several groups in order to obtain efficient emitters in the visible and ultraviolet regions.[7–10] Since III nitrides exhibit huge polarization properties, heterostructures composed of such materials are very interesting for the investigation of strain effects on the optical properties of respective microstructures designed on a mesoscopic scale.

In this paper, we intend to contribute to a deep understanding of the role of strain inhomogeneities on the optical properties of mesoscopic structures through a three-dimensional (3D) model. As it will be shown, cathodoluminescence results as a function of quantum well thickness and the emission linewidth in nanocolumnar structures can be easily explained by means of the aforementioned strain-confinement mechanism. The luminescence intensity decreases as the thickness of the quantum well also decreases, in contrast to previous results in compact material, in which the effect of polarization fields on the wave function overlap plays a major role (i.e., the wave function overlapping decreases for thicker quantum wells). From a practical perspective, these mesoscopic strain properties can have important consequences for the future design of light emitters based on nanocolumnar quantum disks.

This paper is organized as follows. Section 2 introduces the strain-confinement problematic through experimental results found in nanocolumnar AlGaN/GaN quantum disks. A theoretical model explaining in detail the effects of different parameters in the carrier confinement of these mesoscopic structures is presented in Sec. III. Both strain distribution and band structure numerical calculations in two dimensions (2D) are developed to show that the formation of electronic states at the disk periphery is possible under certain conditions. The comparison between experimental and theoretical results allows one to understand the role of peripheral states in carrier recombination dynamics (Sec. IV). Finally, conclusions about the strain-confinement mechanism will be presented in the last section of the manuscript.

II. EXPERIMENTAL RESULTS

Three five-period AlGaN/GaN quantum disks embedded in nanocolumnar structures differing in disk thickness were
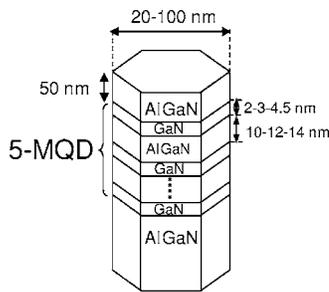
FIG. 1. Structure of the nanocolumns studied.

studied by cathodoluminescence (CL) characterization. For the samples A, B, and C, the thickness of the disks amounts to 2, 3, and 4.5 nm, respectively (see Fig. 1). The samples were grown by rf plasma-assisted molecular-beam epitaxy (MBE) on Si(111) substrates. Details on growth conditions can be found in Refs. 8, 11, and 12. The diameter of the nanocolumns ranges from 20 to 100 nm, with no observable dependence of the disk thickness on diameter.

Basic CL characterization was performed for all samples using a scanning electron microscope (SEM) equipped with an Oxford mono-CL2 and a He-cooling stage operating at temperatures between $T=5$ and 300 K. Results are shown in Fig. 2 representing CL spectra of the samples A, B, and C. The spectra consist of at least two broad lines, where the lines centered between 3.44 and 3.71 eV originate from the respective quantum disks. The higher energy peak corresponds to the emission from the AlGaN barriers. The redshift in the AlGaN transition as the well thickness increases could be explained either by a higher electric field in the barriers or by a strain-induced shift of the AlGaN band edge. Both explanations are possible, since the electric field and the tensile strain generated in the AlGaN barriers increase with disk thickness. We also clearly observe a redshift of the disk transitions with increasing well thickness. Other measurements performed in similar structures with varying Al content also showed a redshift of the transitions for higher Al content, which is consistent with the existence of strong polarization fields.[8] This is the typical behavior of AlGaN/GaN MQW structures.[13,14] On the other hand, since the electron-hole
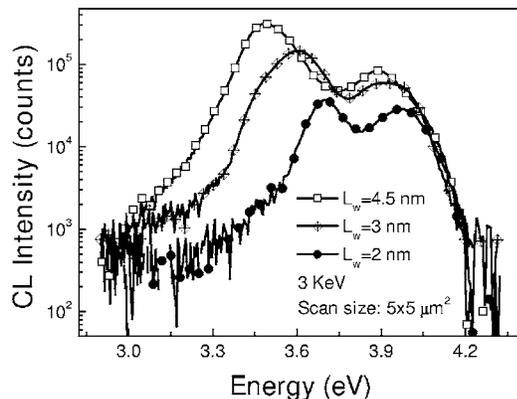

FIG. 2. Cathodoluminescence spectra from samples A (2 nm), B (3 nm), and C (4.5 nm) at 6 K. The beam current used in these measurements amounted to 20 nA.
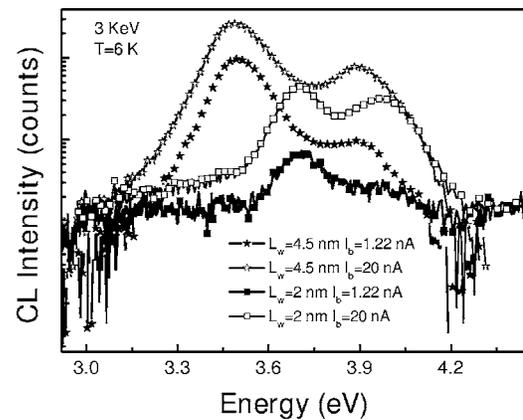

FIG. 3. Power dependence of the CL spectra in samples A (2 nm) and C (4.5 nm).

wave function overlap is larger for narrower quantum wells in common samples, a higher luminescence was expected for sample A. However, the opposite behavior is observed, namely, an anomalous luminescence quenching with decreasing well thickness. This anomalous result motivated a theoretical study of the radiative recombination in these nanocolumnar structures. It is worth noting that CL measurements at different beam energies (not shown) did not change the shape of the spectra, i.e., luminescence spatial variations in the growth direction could not be identified. Although the shape of the CL spectra does not vary, their full width at half maximum (FWHM) increases with increasing electron-beam energies (e.g., the FWHM amounts to 175 meV for 2 keV and 215 meV for 10 keV in sample C). The FWHM was high in all samples, which could be explained, as it will be reported in Sec. 3, considering diameter fluctuations, screening effects, and varying contributions from the periphery and inner parts of the disk.

In Fig. 3, we compare the power dependence of the CL intensity of sample A with the one of sample C. The CL intensity from the quantum wells increases quasi-linearly (in fact sub-linearly) in sample A, while it increases only slightly in sample C. The gradual saturation of the CL intensity as a function of power and disk thickness is representative of the emission of quantum disks embedded in nanocolumnar structures. This behavior is also unusual in intrinsic transitions, pointing to a low density of states for radiative channels, which also depend on the disk thickness.

In order to understand the mechanism governing the luminescence as a function of disk thickness, the physical properties of these nanocolumns were examined. The interface roughness was analyzed by transmission electron microscopy (TEM) showing excellent quality interfaces.[15] The samples were also found to be free of dislocations and planar defects. Since GaN is a binary compound, alloy disorder cannot be invoked for explaining the emission characteristics in the quantum wells. Only point defects or contamination could cause a nonstandard behavior. There are, however, no experimental evidences of large amounts of such defects. Even if point defects are taken into account, the dependence of the CL spectra on the well thickness could not be explained by their presence. Alloy disorder in the barrier could

be responsible for strain fluctuations in the structure tailoring the local electric fields in the quantum disks, but this effect could not explain the dependence of luminescence intensity as a function of disk thickness. Therefore, it is suggested that the mechanism, which is responsible for the luminescence quenching, is characteristic for such structures and is based on an inhomogeneous distribution of the internal strain.

III. THEORETICAL MODEL

Experimental results have shown that the mechanisms involved in the CL (also photoluminescence) of AlGaN/GaN quantum disks differ from the ones of typical multiple-quantum wells. On one hand, the CL intensity quenches with decreasing disk thickness and, on the other hand, the CL intensity saturates at high power densities, affecting more noticeably the thicker disk structures. Characteristic features of these mesoscopic structures are the existence of an inhomogeneous in-plane strain distribution, the lack of extended defects, and the size of the in-plane dimension within a range of a few 10 to a few 100 nm. Here, we study the effect of the inhomogeneous strain distribution on the quantum confinement and on the in-plane electrostatic potential.

The strain has important effects on both the band structure and electrostatic potential through the induced built-in fields.[16–19] At the microscopic scale, the in-plane strain distribution is responsible for an in-plane potential inhomogeneity. Since both the band structure and potential are linked to each other, the effect of strain on the optical properties has to be solved in a self-consistent manner.

A. Strain distribution calculations

Numerical strain calculations were performed for a mesoscopic AlGaN/GaN system grown on a strain-free AlGaN substrate. Although it is hard to establish a clear separation between systems, where the strain inhomogeneity is a determinant factor, typical nanocolumnar nitride quantum disks with diameters in the range of 100 nm or lower can be considered as a good example. The analyzed structure consists of a thin GaN layer (well) sandwiched between two AlGaN layers (barriers). The calculations were based on continuum elasticity theory. The strain field can be thus determined by minimizing the total Helmholtz strain energy functional for a semiconductor material containing composition fluctuations (e.g., a multilayered structure), which is given by[20]

$$E = \int dV \frac{1}{2} \sum_{i=1}^{6} \sum_{j=1}^{6} C_{ij}[\varepsilon_i(r) - \varepsilon_i^0(r)][\varepsilon_j(r) - \varepsilon_j^0(r)], \quad (1)$$

where ε_i are the elastic strain components, ε_i^0 are the local intrinsic strain components originating from the lattice mismatch between the barrier and well materials, and C_{ij} are the fourth-ranked elastic stiffness components. Voigt notation has been used in Eq. (1) to express the strain components. Equation (1) can be further simplified, since we are dealing with hexagonal materials.[21] Symmetry considerations lead to only five nonvanishing, independent elastic stiffness components, namely, C_{11}, C_{12}, C_{13}, C_{33}, and C_{44}. ε_i^0 components can be calculated as $\varepsilon_1^0 = \varepsilon_2^0 = (a_{AlGaN} - a_{GaN})/a_{GaN}$, $\varepsilon_3^0 =$

$-2C_{13}\varepsilon_1^0/C_{33}$, $\varepsilon_4^0 = \varepsilon_5^0 = \varepsilon_6^0 = 0$ in the GaN regions (wells), as well as $\varepsilon_1^0 = \varepsilon_2^0 = \varepsilon_3^0 = \varepsilon_4^0 = \varepsilon_5^0 = \varepsilon_6^0 = 0$ in the AlGaN regions (barriers), where a_{GaN} and a_{AlGaN} are the GaN and AlGaN lattice parameters, respectively. The elastic strain components can be written in terms of the displacement vector $\mathbf{u(r)}$ as

$$\varepsilon_{ij}(r) = \frac{1}{2}\left[\frac{\partial u_i(r)}{\partial r_j} + \frac{\partial u_j(r)}{\partial r_i} \right], \quad (2)$$

where i and j run over x, y, and z. The correspondence between the notation used in Eq. (1) and the one of Eq. (2) is as follows: $\varepsilon_1 = \varepsilon_{xx}$, $\varepsilon_2 = \varepsilon_{yy}$, $\varepsilon_3 = \varepsilon_{zz}$, $\varepsilon_4 = 2\varepsilon_{yz}$, $\varepsilon_5 = 2\varepsilon_{zx}$, and $\varepsilon_6 = 2\varepsilon_{xy}$. Substituting Eq. (2) into Eq. (1), the energy can be readily minimized with respect to $\mathbf{u(r)}$. This problem can be treated in two dimensions given the symmetry of the nanocolumnar structure in the in-plane direction, whereas the numerical solution in the entire space requires some type of mesh. A two-dimensional (2D) rectangular mesh was used in the numerical calculations with the axis along the $[2\bar{1}\bar{1}0]$ and $[0001]$ directions (x and z directions, respectively). The displacements were discretized at the nodes of the mesh, whereas their first derivatives were obtained by finite differences. In order to avoid unphysical oscillatory solutions, Pryor et al.[22] suggested to average the strain energy over all permutations of forward and backward differences (eight in the case of three difference operators and four in the case of two difference operators). The resulting average energies so discretized were minimized using standard algorithms.

Dirichlet boundary conditions were implemented in the lateral, upper, and lower surfaces. We imposed that the material is relaxed at these surfaces, so $u=0$ at the boundary of the whole structure. It is worth noting that zero displacement is referred to the strain-free lattice parameter in each material, but in the case of using a single displacement vector to represent the strain field in the whole mesh, proper corrections must be applied. Derivative boundary conditions would be more appropriate to calculate the real strain field. Nevertheless, calculations setting $u=0$ at the boundary of the structure are not worsening the accuracy in this case at the expense of a better convergence.

The converse piezoelectric effect is not included in Eq. (1). In order to incorporate the converse piezoelectric effect, a self-consistent approach is required which considers the strain energy (derived from a fully coupled equation of state for piezoelectric materials) as well as the Schrödinger and Poisson equations. Therefore, the strain field will be slightly overestimated in our calculations, merely affecting the quantitative agreement but not the main conclusions of the proposed theory. For instance, for an infinite diameter quantum disk structure consisting of 4.5-nm-thick GaN disks and 14-nm-thick AlGaN barriers (28% Al), the magnitude of the electric field in the disk region changed from 2.29 MV/cm for a semicoupled model to 2.18 MV/cm for a fully coupled model (see Ref. 23 for a deeper discussion). The quantitative agreement worsens as the strain increases (e.g., for a higher Al content). An estimation of the electromechanical coupling for quantum disks with infinite diameter was used to determine the real ε_0 strain parameters, as experimental and calculated values were compared, resulting in a corrected semi-
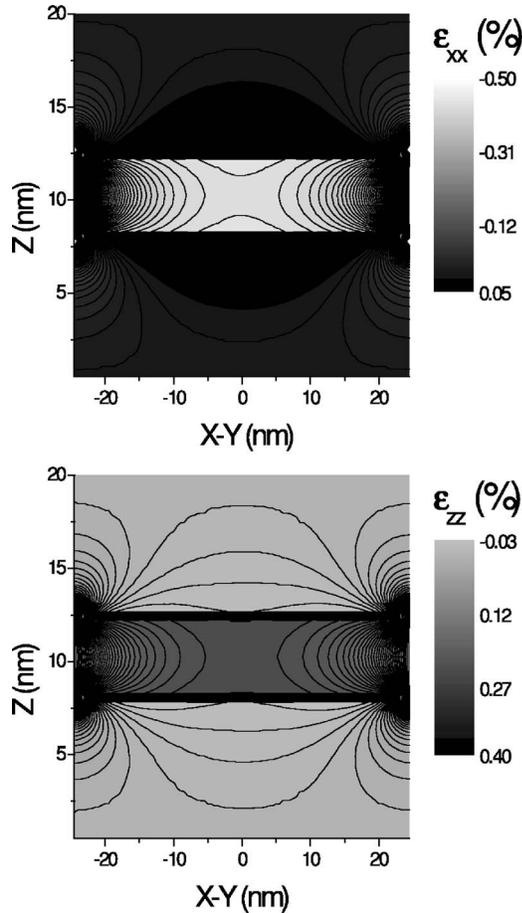
FIG. 4. In-plane strain distribution in the GaN layer for an AlGaN(8 nm)/GaN(4.5 nm) MQD structure with a diameter of 50 nm. Top graph shows the strain distribution of ε_{xx}, whereas bottom graph shows the strain distribution of ε_{zz}.

FIG. 5. In-plane lattice constant as a function of the distance from the center of the GaN disk. The various curves in (a) represent disks differing in diameter (25–100 nm) for a fixed disk thickness of 4.5 nm. The various curves in (b) represent disks differing in thickness (1.5–7.5 nm) for a fixed diameter of 50 nm of the nanocolumnar structures. The Al content used in these calculations was 20%.

coupled model. The slight overestimation of the electric field in the quantum disks produces a redshift of the fundamental transition, which increases as a function of disk thickness.

Figure 4 shows the 2D strain distribution calculated by the procedure described above. We can notice that the strain inhomogeneity mainly affects the GaN film and surrounding areas, as expected considering the used boundary conditions. Peripheral regions are less strained than inner ones, where the local strain in the inner regions is slightly lower than the one generated by the lattice mismatch between the AlGaN substrate and the GaN film. As it will be shown below, the strain inhomogeneity cannot be neglected to understand the optical and electrical properties of structures like this. The effects of the structure geometry (i.e., column diameter and disk thickness) and the Al composition on the strain distribution become visible considering the in-plane strain as a function of the distance from the center of the disk, as shown in Fig. 5. Clearly, the portion of the quantum disks which is affected by the strain inhomogeneity decreases as their diameter increases. Moreover, the maximum strain reached at the center of the quantum disk decreases with decreasing diameter. The opposite dependence was found, when the disk thickness was changed from 1.5 to 7.5 nm for a fixed diameter, as can be seen in Fig. 5(b). Thicker disks presented lower maximum values of strain and, at the same time, the effect of lateral strain relaxation on the strain inhomogeneity was more important. In the case of disks thicker than their barriers, the strain could be even reversed, i.e., barriers would be more strained than disks. Transmission electron microscope (TEM) investigations revealed a bowing in the lateral surfaces of AlGaN-GaN interfaces, confirming our results of the strain field calculations.[15] On the other hand, a higher Al composition in the barriers leads to a higher degree of strain at the center. The effect of strain inhomogeneity and, therefore, its role on optical and electrical properties, will be more significant for samples with higher Al content.

B. Electronic band structure calculations

The most interesting results appear as a consequence of the interplay between polarization-induced fields and deformation potentials under an inhomogeneous strain distribution. Since polarization fields cause a confinement of the carriers at the center of the disk, whereas deformation potentials tend to confine the carriers at the periphery of the disk (compressive strain), the net result will be dependent on the magnitude of the parameters involved in its determination. Intrinsic parameters are the conduction and valence band de-

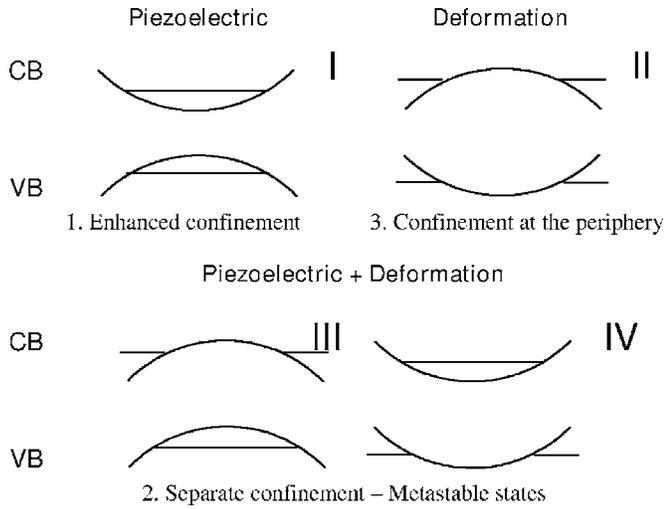FIG. 6. Potential for the in-plane directions of a GaN/AlGaN quantum disk. For I (II), the piezoelectric (deformation) potential determines the net potential of both conduction and valence band. For III (IV), the piezoelectric potential determines only the net potential of the valence (conduction) band, whereas the deformation potential determines the net potential of the conduction (valence) band.

formation potentials, the elastic and piezoelectric constants, and the column diameter. Extrinsic parameters are the Al composition of the barriers and the disk thickness. Possible scenarios are shown in Fig. 6. For case I (II) the piezoelectric (deformation) potential determines the net potential of both conduction and valence bands. Hence, in case I (II), ground electronic states are preferably formed at the center (periphery) of the disk. The situation is different in case III (IV), where the piezoelectric (deformation) potential determines only the net potential of the valence band, whereas the deformation (piezoelectric) potential determines the net potential of the conduction band. Now, ground electronic states for electrons and holes can be spatially separated in such a way that lowest energy transitions exhibit reduced oscillator strengths. Since the air-material interface imposes an infinite barrier for calculation purposes, the in-plane bending at the periphery in cases II, III, and IV must be large enough to allow for a formation of quantized levels. Consequently, states at the center of the disk will be present at higher energies than the ground electronic level for all cases, whereas additional quantization at the periphery will be possible for both conduction and valence band, conduction band only, and valence band only in cases II, III, and IV, respectively.

Although the potential in the quantum disk is the result of complex interactions between structure parameters, it is feasible to establish a dependence of the expected behavior on the disk thickness for a given Al composition in the barriers. The potential drop in a quantum disk due to polarization fields increases linearly with its thickness for large, built-in electric fields. Therefore, it is expected that piezoelectric effects prevail over deformation potential modifications in thicker quantum disks (case I in Fig. 6). The opposite situation, i.e., case II, is more probable for very thin quantum disks, being cases III and IV for intermediate values of the

disk thickness. The effect of spontaneous polarization is constant in the in-plane direction for a uniform Al composition in the barriers. The effect of strain on the confinement of carriers is what has been called piezoelectric strain confinement.

The electrostatic potential is also affected by the band bending of surface potentials and the doping levels. Samples studied have not been doped intentionally. Thus, the main contribution to the in-plane electrostatic potential distribution in the quantum disks is given by both the piezoelectric and the deformation potentials. The electric fields in the jth layer (either barrier or quantum disk) can be calculated as

$$E_j = \frac{\sum_k (P_k - P_j) l_k / \kappa_k}{\kappa_j \sum_k l_k / \kappa_k}, \tag{3}$$

assuming that the space charge region cannot range from lateral surfaces to the center of the disk for such doping levels. In Eq. (3), P_k, l_k, and κ_k are the total transverse polarization, the thickness, and the dielectric constant of the layer k, where k runs on all layers in the structure. High doping levels have two different effects on the in-plane potential distribution. Firstly, the piezoelectrically induced electric fields are screened, resulting in a more important effect of the deformation potentials. Secondly, lateral band bending can occur. Very different pictures could be obtained for high doping values, but our analysis is focused on the unintentionally doped case.

A 2D Schrödinger solver was developed to study the in-plane carrier distribution. For calculation purposes, the nanocolumnar structure was considered to have cylindrical symmetry, i.e., the results are extended to the 3D case. Assuming parabolic conduction band dispersions, an effective-mass equation for a single particle is given as

$$\left[-\frac{\hbar^2}{2m^{\parallel}} \frac{1}{r} \frac{\partial}{\partial r} \left(r \frac{\partial}{\partial r} \right) - \frac{\hbar^2}{2m^{\perp}} \frac{\partial^2}{\partial z^2} + V(r,z) \right] \Phi = E \Phi, \tag{4}$$

where V is the potential including the effects of built-in fields and the strain-induced band structure modification. Parameters used in the calculations were extracted from recommended values of Ref. 24. A summary of the parameters used is also presented in Table I.

The solution of Eq. (4) was implemented using the finite-element method.[25,26] The elements were based on a nine-noded rectangular scheme. Biquintic Hermitian shape functions were used to allow for the inclusion of derivative continuity at the nodes. Vanishing boundary conditions were imposed at the free lateral surface, requiring boundary conditions of continuity of the envelope function and continuity of the effective mass derivative at the well-barrier interface. The potential profile was obtained, taking into account the polarization field distribution induced by the strain field determined from Eq. (1). The contribution of spontaneous polarization to the potential V^{sp} was calculated numerically by

TABLE I. Physical parameters for GaN and AlN. The ternary parameters were obtained by linear interpolation between corresponding values for GaN and AlN materials. Valence band effective-mass parameters (A_i) were used to determine the heavy hole effective masses for both longitudinal (∥) and transverse (⊥) directions.

Parameters	GaN	AlN
a_{lc} (Å) at $T=300$ K	3.189	3.112
E_g (eV)	3.507	6.23
$m_e^{\parallel}$	0.20	0.28
$m_e^{\perp}$	0.20	0.32
A_1	−6.56	−3.95
A_2	−0.91	−0.27
A_3	5.65	3.68
A_4	−2.83	−1.84
A_5	−3.13	−1.95
A_6	−4.86	−2.91
a_{cz} (eV)	−6.5	−9
a_{ct} (eV)	−11.8	−9
D_1 (eV)	−3.0	−3.0
D_2 (eV)	3.6	3.6
D_3 (eV)	8.82	9.6
D_4 (eV)	−4.41	−4.8
D_5 (eV)	−3.6	−4.0
D_6 (eV)	−5.1	−5.1
C_{11} (GPa)	390	396
C_{12} (GPa)	145	137
C_{13} (GPa)	106	108
C_{33} (GPa)	398	373
C_{44} (GPa)	105	116
e_{13} (C/m^2)	−0.35	−0.50
e_{33} (C/m^2)	1.27	1.79
e_{15} (C/m^2)	−0.3	−0.48
P_{sp} (C/m^2)	−0.029	−0.081

$$V^{sp}(\vec{r}) = \frac{1}{4\pi\varepsilon} \int \int \frac{\rho_s(\vec{r}')}{|\vec{r} - \vec{r}'|} ds', \qquad (5)$$

where ρ_s is the density of bound charges induced by the spontaneous polarization field discontinuity in the AlGaN-GaN interface, i.e., $\nabla P = -\rho_s$. As a result of the finite size in the in-plane direction, edge effects affect both the maximum potential drop within the quantum disks and its in-plane dependence. These effects are more important in the case of the piezoelectric polarization contribution to the potential V^{pz}, since the strain distribution determines the spatial dependence of piezoelectric fields. The piezoelectrically induced potential was given by

$$V^{pz}(\vec{r}) = \frac{1}{4\pi\varepsilon} \int \int \int \frac{\vec{P}(\vec{r}) \cdot (\vec{r} - \vec{r}')}{|\vec{r} - \vec{r}'|^3} d^3 r'. \qquad (6)$$

Since ε_{yz} and ε_{zx} are small, V^{pz} was mainly determined by the polarization field component in the growth direction, i.e.,

TABLE II. Nominal values of structural parameters of five-period AlGaN/GaN MQW samples used in simulations. L_{cl} is the thickness of the cap layer. Samples are referred in the text through the well thickness (e.g., sample C is the sample with $L_w=4.5$ nm, regardless of the barrier thickness). The experimentally investigated samples A, B, and C exhibit a nominal well thickness of 2, 3, and 4 nm, respectively, with a fixed barrier thickness of 10 nm.

Sample	L_w (nm)	L_b (nm)	L_{cl} (nm)	% Al
A	2	8–12–14	50	28
B	3	8–12–14	50	28
C	4.5	8–12–14	50	28

$P_z = 2(e_{13} - e_{33} C_{13}/C_{33})\varepsilon_{xx}$, whereas e_{ij} are the piezoelectric stress constants.[27] Lastly, V was also affected by the strain-induced band-gap modification. Both conduction and valence bands were shifted under compressive strain as

$$\Delta E_c = a_{cz}\varepsilon_{zz} + a_{ct}(\varepsilon_{xx} + \varepsilon_{yy}), \qquad (7)$$

$$\Delta E_v = (D_1 + D_3)\varepsilon_{zz} + (D_2 + D_4)(\varepsilon_{xx} + \varepsilon_{yy}), \qquad (8)$$

where a_{ci} and D_i denote the deformation potentials for the conduction and valence band, respectively. The condition given by Eq. (3) was imposed in the calculation of the 3D potential profile for the whole multiquantum disk region through a proper definition of the boundary conditions. The electric field in the barriers so determined was opposite to that in the quantum disk. Therefore, the potential drop in each quantum disk was lower than that calculated by Eqs. (5)–(8). Moreover, the electric field in the barriers was not uniform, partially compensating the edge effect and the in-plane strain inhomogeneity.

Samples A and C (structural parameters used in the calculations are listed in Table II) were studied following the proposed scheme without neglecting the in-plane dependence. The calculations were carried out under equilibrium conditions for one arbitrary quantum disk. Results are shown in Figs. 7 and 8, as well as in Table III.[28] We have adopted a particular nomenclature to designate the electron and hole states at the center and periphery of the disk. The first subscript references the level of the quantization in the growth direction, whereas the second subscript references the level of the quantization in the in-plane direction. In the cases where states are also quantized at the periphery, a third subscript is used related to a new set of states with its own in-plane and growth direction levels.

Some general remarks about calculation results can be summarized as follows. First, the in-plane confinement is weaker than the confinement in the growth direction. This result is easily explained, since the column diameter is more than one order of magnitude larger than the well thickness. Therefore, the first quantized levels are close in energies and correspond to the same quantization in the growth direction. Secondly, transition energies obtained for $L_w=2$ nm agree with reported experimental values, whereas the transition energies obtained for $L_w=4.5$ nm are low compared with those values. If screening of built-in electric fields is also taken
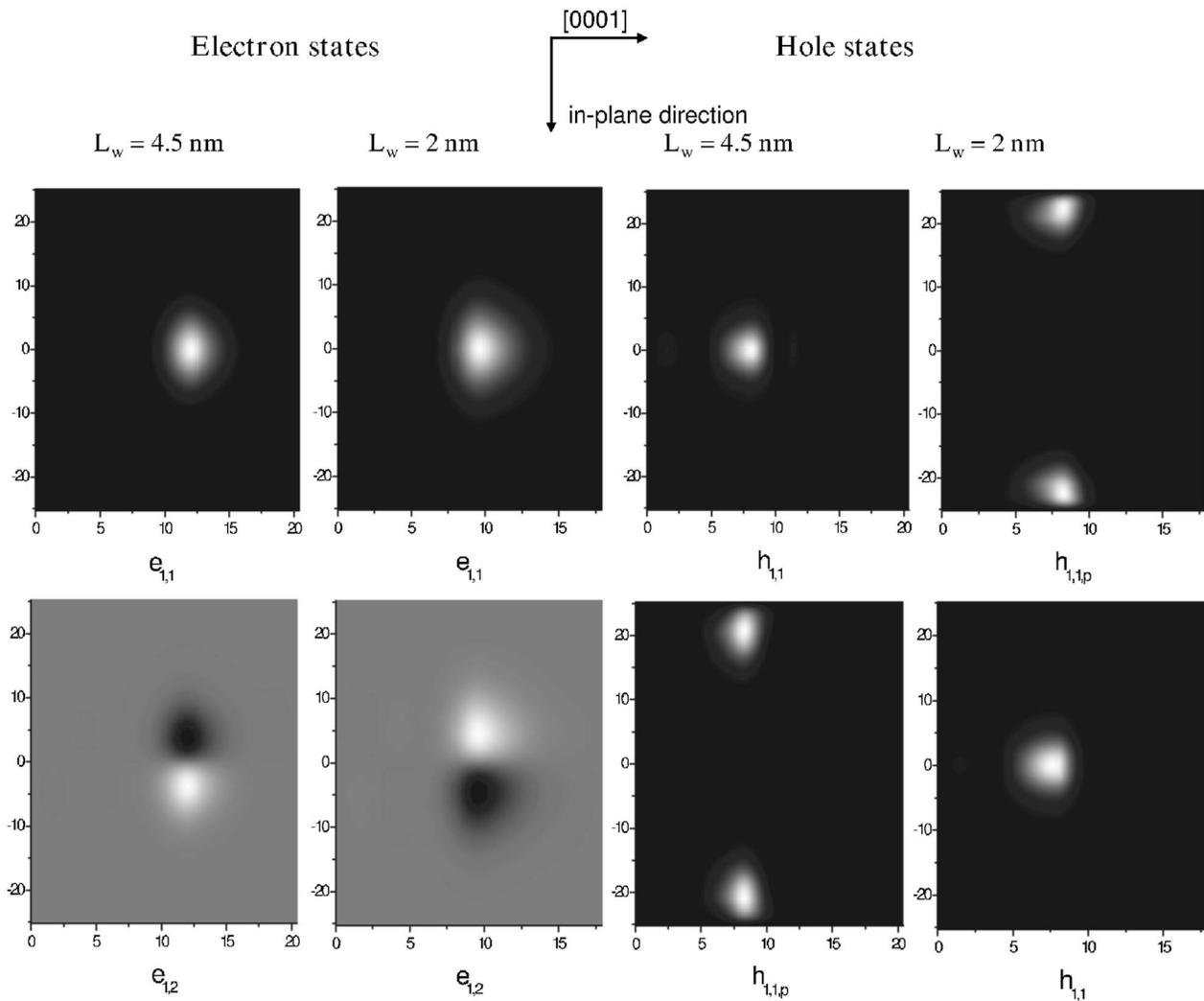
FIG. 7. Lateral distribution of calculated electron and hole wave functions for a generic quantum well in a nanocolumnar structure, taking an inhomogeneous strain distribution in the in-plane direction into account. Two cases differing in the well thickness (2 and 4.5 nm) are considered. Disk diameter amounts to 50 nm. Number subscripts stand for quantization in the growth and lateral direction. Subscript p refers to peripheral states. Axis units are in nanometers.

into account, transition energies for $L_w=4.5$ nm are expected to be blue-shifted according to experimental data. Moreover in Table II, well and barrier thicknesses are nominal values and small corrections can result in important transition energy deviations, as it will be shown below. Thirdly, electrons are confined at the center, whereas holes can be confined at the center or at the periphery. The lateral confinement is the result of the in-plane potential distribution. Depending on the potential drop from the center to the lateral side of the column, the number of confined states at the periphery can be higher than one. Quantized levels induced at the periphery of the disk will be called hereafter peripheral states. Finally, recombination times for ground transitions at the center of the disk are one order of magnitude higher for $L_w=4.5$ nm than for $L_w=2$ nm, as expected by the larger carrier separation in the growth direction in the first case.

Figure 7 and Table III show that both the confinement of electron and hole ground states are produced at the center of the disk for sample C with $L_w=4.5$ nm and $L_b=14$ nm (case

I of Fig. 6). However, as predicted by the model discussed, the situation is different for sample A ($L_w=2$ nm and $L_b=14$ nm), where the ground level of holes appears at the periphery of the disk. While holes are preferably distributed at the periphery, electrons tend to stay at the center of the disk (case IV of Fig. 6). This result implies an important reduction of the wave function overlap of the fundamental transition (the less energetic one). Nevertheless, hole states at the center and at the periphery are formed for both disk thicknesses, so recombination at the center of the disk and crossed transitions between central and peripheral states are also found in samples A and C, respectively.

The effect of barrier thickness has also been investigated by means of numerical calculations. Figure 8 shows the effect of barrier thickness on the hole confinement for $L_w=4.5$ nm as a consequence of the condition imposed by Eq. (3). As the barrier thickness decreases, the potential for holes at the periphery also decreases. Thus, holes will tend to be confined at the periphery already for $L_b=12$ nm, as shown in

Hole states

FIG. 8. Lateral distribution of calculated hole wave functions for a generic quantum well in a nanocolumnar structure, taking an inhomogeneous strain distribution in the in-plane direction into account. Two cases differing in the barrier thickness (8 and 12 nm) are considered. Disk thickness and diameter amount to 4.5 and 50 nm, respectively. Number subscripts stand for quantization in the growth and lateral direction. Subscript p refers to peripheral states. Axis units are in nanometers. The bottom diagram shows the spatially varying ground levels in the valence band for 8, 12, and 14 nm barrier thicknesses. The energy values in this diagram are referred to the maximum potential in the valence band.

TABLE III. Calculated transition energies and recombination times of the lowest states at the center and periphery of the disk for the wave functions in Fig. 7. Recombination times were normalized to the ideal square well recombination time, $\tau_0 \approx 0.4$ ns.[a] The first hole state at the periphery was the second eigenvalue for sample C and the first for sample A.

$L_w = 2$ nm (sample A)			
E_c (% inside QW)	E_v (% inside QW)	$E_{transition}$ (eV)	τ/τ_0
$E_{e1,1}$ (52%)	$E_{hh1,1}$ (24%)	3.704	3.51
$E_{e1,1}$	$E_{hh1,1,p}$ (53%)	3.693	3732
$E_{e1,2}$ (52%)	$E_{hh1,1}$	3.727	735
$E_{e1,2}$	$E_{hh1,1,p}$	3.716	675716
$L_w = 4.5$ nm (sample C)			
E_c (% inside QW)	E_v (% inside QW)	$E_{transition}$ (eV)	τ/τ_0
$E_{e1,1}$ (66%)	$E_{hh1,1}$ (45%)	3.183	41.5
$E_{e1,1}$	$E_{hh1,1,p}$ (63%)	3.190	43007
$E_{e1,2}$ (67%)	$E_{hh1,1}$	3.216	51408
$E_{e1,2}$	$E_{hh1,1,p}$	3.223	404269

[a]Reference 28.

Fig. 8, i.e., the hole ground state will appear at the periphery. It is important to emphasize that for $L_b = 12$ nm, the separation between hole ground state at the center and at the periphery is small (some meV), while it is as large as 150 meV for $L_b = 8$ nm (cf. Fig. 8). Hence, the hole population distribution at the periphery will be more noticeably for thinner barrier structures. On the other hand, transition energies of states at the center increase monotonously until 3.54 eV for $L_b = 8$ nm. The large difference between experimental and calculated values in Table III could be explained for a barrier thinner than the nominal used in the calculations (e.g., 10 nm instead of 14 nm). Although thickness deviations were confirmed by TEM, the difference was lower than 15%, so other factors such as carrier screening should be also considered.

The effects of the disk diameter, the induced photogenerated screening, and the number of well layers on luminescence broadening were studied. In the piezoelectric strain-confinement framework, fluctuations of the disk diameter lead to large linewidths of the photoluminescence transitions. Quantum disks with sufficiently large diameters can be considered as fully strained quantum wells. On the other hand, the well material is nearly fully relaxed for small diameter disks [see Fig. 5(a)]. Even the contribution of spontaneous polarization to the potential decreases due to the edge effects for small diameter disks. Therefore, the transition energies are blue-shifted by large amounts as the diameter decreases. The in-plane strain is responsible for an important spectral broadening of the fundamental transition on the order of 100 meV.

The effect of screening on optical properties can be more important than in common situations. Since confinement for electrons and holes can be different in the in-plane direction, charge accumulation can be nonuniform across the quantum disk. In principle, states with a reduced wave function over-
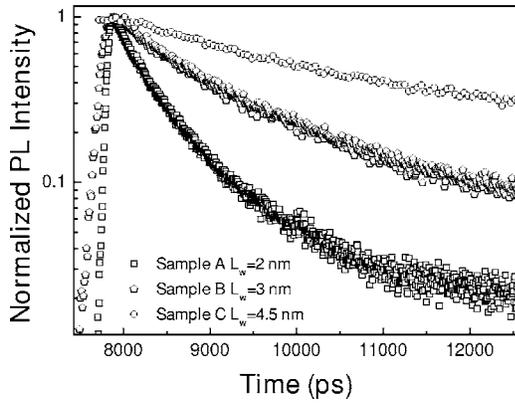
FIG. 9. Time-resolved photoluminescence for samples A, B, and C. The temperature amounted to 7 K. The three samples showed the expected nonexponential decay dynamics.

lap accumulate more carriers, leading to a blueshift of the transition energies. The use of multiple quantum disks embedded in the nanocolumnar structure implies a broadening of the luminescence spectra when doping levels lead to a band bending within the top and lateral near-surface regions (i.e., nonperiodic boundary conditions). Therefore, the effect of polarization fields for multiple quantum disk structures also leads to a broadening of the luminescence since the potential distribution depends on disk number.

Theoretical results point to a complex behavior of the luminescence of such structures. The luminescence spectra are broadened due to inhomogeneous strain. New quantized states not present in macroscopic quantum wells allow for a *spatially dependent* confinement of carriers. The in-plane carrier distribution between states at the periphery and center of the disk is especially important. The effect of the in-plane carrier distribution is well accounted by the disk thickness dependence (both well and barrier). Below a critical well or barrier thickness, electrons and holes are confined in different disk areas for the ground state. Experimental results pointing to a quenching of luminescence in thin disk superlattices were reported in similar structures, confirming the above hypothesis as a possible explanation.[29] Recently, it was also found in Raman experiments on GaN/AlN multiple-quantum-disk nanocolumnar structures that confined, quasiconfined, and interface modes not present in GaN/AlN superlattice films were observed. These modes were tentatively assigned to quantization along the radial (in-plane) direction of the disk.[30]

IV. DISCUSSION

The strain-confinement model described in this work can explain the luminescence results obtained in the structures analyzed in Sec. II. Besides, it has additional implications. For decreasing well thickness, the observed luminescence quenching is due to the fact that peripheral states can be formed so that the in-plane potential can separate carriers. Since transitions between states at the center and ones at the periphery exhibit reduced oscillator strength, long recombination times and low luminescence efficiencies are expected.
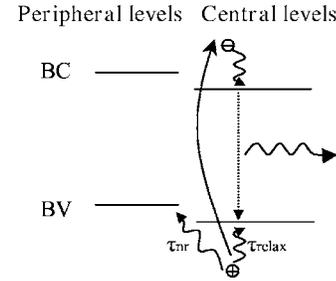

FIG. 10. Model of carrier capture and relaxation in the quantum disks for sample A (narrow quantum well). Luminescence intensity is strongly affected by the scattering of holes toward the periphery.

Thus, we studied the carrier recombination dynamics to learn more about the role of these peripheral states.

Time-resolved photoluminescence (TRPL) was carried out using the third harmonic of a femtosecond tunable Ti-:sapphire laser. The repetition rate was low enough to avoid memory effects between pulses. Figure 9 shows the results for low temperature, corresponding to the emission of quantum disks for samples A, B, and C. Comparable results were obtained in a similar set of samples.[31] The typical nonexponential behavior of AlGaN/GaN quantum wells associated with polarization field effects is found. In this case, the electron-hole wave function overlap changes dynamically as a function of the number of carriers due to the electric field screening. It is remarkable to mention that long times of 2, 7, and 20 ns in samples A, B, and C, respectively, were determined for an average recombination time given by

$$\tau_r = \int f(t)t\,dt, \tag{9}$$

where $f(t)$ is the normalized recombination function as measured by TRPL. The experimental data are in good agreement with the theoretical calculations presented in Table III (1.4 and 16.6 ns in samples A and C, respectively).

These results lead us to the conclusion that spatially separated states are practically dark (i.e., optically inactive). Therefore, a possible recombination model for the cases II, III, and IV of Fig. 6 could be the one shown in Fig. 10, where the luminescence quenching is based on the relaxation process of the carriers followed after excitation. Carriers, which are scattered to the states at the center of the disk (or periphery in case II), exhibit a higher CL (also photoluminescence) efficiency compared with that corresponding to crossed transitions. As the energy of the states at the periphery is lower, more carriers are attracted to the periphery regions, resulting in an overall decrease of the radiative efficiency. In addition to the fact that states at the periphery exhibit a reduced oscillator strength, surface recombination can also work as a nonradiative channel in cases III and IV.

V. CONCLUSIONS

A 3D model has been presented which accounts for the carrier distribution in mesoscopic devices in the in-plane direction as a result of lateral strain inhomogeneities created in

lattice-mismatched structures. This work is part of what has been called wave-function engineering, describing a new mechanism of carrier confinement for inhomogeneous strained layers known as strain confinement. Theoretical results have shown the existence of confined states spatially separated in the in-plane direction at the center and periphery of these structures. The theory has been applied to AlGaN/GaN nanocolumnar quantum disks, providing an explanation to the main characteristics of luminescence, especially the broadening, the behavior as a function of well and barrier thicknesses, and the long recombination times of certain parts of the luminescence spectra. The design of new structures must be carried out carefully, taking strain-induced effects into account, mainly in what refers to barrier and well thicknesses, lateral dimensions, and doping concentration.

From theoretical investigations we conclude that the carrier confinement at the center of the disk improves for wider and thicker disk wells and barriers. In the case of AlGaN/GaN nanocolumnar quantum disks, hole states formed at the periphery exhibit reduced oscillator strength. The radiative efficiency of these states additionally decreases by nonradiative recombination via surface states, leading to a significant reduction in overall luminescence.

*Electronic address: crivera@die.upm.es

[1] Z. H. Wu, X. Mei, D. Kim, M. Blumin, H. E. Ruda, J. Q. Liu, and K. L. Kavanagh, Appl. Phys. Lett. **83**, 3368 (2003).

[2] M. Nishioka, S. Tsukamoto, Y. Nagamune, T. Tanaka, and Y. Arakawa, J. Cryst. Growth **124**, 493 (1992).

[3] Z. L. Wang, X. Y. Kong, and J. M. Zuo, Phys. Rev. Lett. **91**, 185502 (2003).

[4] H. Won Seo, S. Yong Bae, J. Park, H. Yang, K. Soo Park, and S. Kim, J. Chem. Phys. **116**, 9492 (2002).

[5] M. Sugawara, Phys. Rev. B **51**, 10743 (1995).

[6] J. Ristić, C. Rivera, E. Calleja, S. Fernández-Garrido, M. Povoloskyi, and A. Di Carlo, Phys. Rev. B **72**, 085330 (2005).

[7] J. Ristić, E. Calleja, A. Trampert, S. Fernández-Garrido, C. Rivera, U. Jahn, and Klaus H. Ploog, Phys. Rev. Lett. **94**, 146102 (2005).

[8] J. Ristić, E. Calleja, M. A. Sánchez-García, J. M. Ulloa, J. Sánchez-Paramo, J. M. Calleja, U. Jahn, A. Trampert, and K. H. Ploog, Phys. Rev. B **68**, 125305 (2003).

[9] M. Yoshizawa, A. Kikuchi, N. Fujita, K. Kushi, H. Sasamoto, and K. Kishino, J. Cryst. Growth **189/190**, 138 (1998).

[10] Y. S. Park, C. M. Park, D. J. Fu, T. W. Kang, and J. E. Oh, Appl. Phys. Lett. **85**, 5718 (2004).

[11] E. Calleja, M. A. Sánchez-García, F. J. Sánchez, F. Calle, F. B. Naranjo, E. Muñoz, U. Jahn, and K. Ploog, Phys. Rev. B **62**, 16826 (2000).

[12] J. Ristić, M. A. Sánchez-García, E. Calleja, J. Sánchez-Páramo, J. M. Calleja, U. Jahn, K. H. Ploog, Phys. Status Solidi A **192**, 60 (2002).

[13] N. Grandjean, B. Damilano, S. Dalmasso, M. Leroux, M. Laügt, and J. Massies, J. Appl. Phys. **86**, 3714 (1999).

[14] P. Lefebvre, J. Allègre, B. Gil, H. Mathieu, N. Grandjean, M. Leroux, J. Massies, and P. Bigenwald, Phys. Rev. B **59**, 15363 (1999).

[15] J. Ristić, E. Calleja, S. Fernández-Garrido, A. Trampert, U. Jahn, K. H. Ploog, M. Povoloskyi, and A. Di Carlo, Phys. Status Solidi A **202**, 367 (2005).

[16] F. Bernardini and V. Fiorentini, Phys. Rev. B **57**, R9427 (1998).

[17] S.-H. Wei and A. Zunger, Phys. Rev. B **60**, 5404 (1999).

[18] W. W. Chow and S. W. Koch, in *GaN and Related Materials II*, edited by S. J. Pearton (Gordon and Breach Science, Amsterdam, 2000).

[19] V. Ranjan, G. Allan, C. Priester, and C. Delerue, Phys. Rev. B **68**, 115305 (2003).

[20] I. P. Ipatova, V. G. Malyshkin, and V. A. Shchukin, J. Appl. Phys. **74**, 7198 (1993).

[21] J. F. Nye, *Physical Properties of Crystals* (Oxford University Press, New York, 1957).

[22] C. Pryor, J. Kim, L. W. Wang, A. J. Williamson, and A. Zunger, J. Appl. Phys. **83**, 2548 (1998).

[23] B. Jogai, J. D. Albrecht, and E. Pan, Semicond. Sci. Technol. **19**, 733 (2004).

[24] I. Vurgaftman, J. R. Meyer, and L. R. Ram-Mohan, J. Appl. Phys. **89**, 5815 (2001).

[25] O. C. ZienKiewicz, *The Finite Element Method*, 3rd ed. (McGraw-Hill, New York, 1977).

[26] L. R. Ram-Mohan, *Finite Element and Boundary Element Applications to Quantum Mechanics* (Oxford University Press, Oxford, 2002).

[27] B. Jogai, J. Appl. Phys. **90**, 699 (2001).

[28] The radiative recombination τ_0 is given by $\tau_0 = [(2e^2 \eta p_{cv} G / 3 \pi \varepsilon_0 \hbar^2 c^3 m^2) E_g]^{-1}$, where the symbols have the same meaning as in B. K. Ridley, Phys. Rev. B **41**, 12190 (1990). See also W. P. Dumke, Phys. Rev. **132**, 1998 (1963); and R. Klann *et al.*, Phys. Rev. B **52**, R11615 (1995).

[29] J. H. Na, R. A. Taylor, J. H. Rice, J. W. Robinson, K. H. Lee, Y. S. Park, C. M. Park, C. M. Park, and T. W. Kang, Appl. Phys. Lett. **86**, 083109 (2005).

[30] T. Sekine, S. Suzuki, H. Kuroe, M. Tada, A. Kikuchi, and K. Kishino, e-J. Surf. Sci. Nanotechnol. **4**, 227 (2006).

[31] M. Zamfirescu, M. Abbarchi, M. Gurioli, A. Vinattieri, J. Ristić, and E. Calleja, Phys. Status Solidi C **2**, 822 (2005).